Nano Research

Open Access

Research Article

Biomimetic calcium carbonate-calcium phosphate composite films with tunable cytological behaviors

Yu-Lu Yang[1,§], Xiu-Wu Guo[1,2,§], Yu-Feng Meng[1], Wen-Zhi Zhang[2] ✉, Li-Bo Mao[1] ✉, and Shu-Hong Yu[1,3] ✉

[1] *Department of Chemistry, Institute of Biomimetic Materials and Chemistry, Anhui Engineering Laboratory of Biomimetic Materials, New Cornerstone Science Laboratory, Division of Nanomaterials and Chemistry, Hefei National Research Center for Physical Sciences at the Microscale, University of Science and Technology of China, Hefei 230026, China*

[2] *Department of Orthopedics, The First Affiliated Hospital of USTC, Division of Life Sciences and Medicine, University of Science and Technology of China, Hefei 230001, China*

[3] *Institute of Innovative Materials, Department of Materials Science and Engineering, Department of Chemistry, Southern University of Science and Technology, Shenzhen 518055, China*

§ *Yu-Lu Yang and Xiu-Wu Guo contributed equally to this work.*

Cite this article: *Nano Research*, **2025**, *18*, 94907055. https://doi.org/10.26599/NR.2025.94907055

ABSTRACT: Calcium phosphate salts, which have a similar composition with the mineral phase in natural bone, have been extensively studied for their applications in bone regeneration. However, another calcium-based mineral, calcium carbonate, which is also frequently found in biological materials, is seldom considered for this purpose despite their high biocompatibility and bioactivity. Herein, we report the performance of five types of biomimetic mineral films that are fabricated via the mineralization of calcium carbonate and calcium phosphate on chitin. These films have different *in vitro* degradation dynamics because of their varied stability. They also show distinct surface roughness, modulus and hardness. Cytological analyses reveal that, although these films all display high biocompatibility, they exhibit diverse osteogenic differentiation behavior, which can be attributed to their respective physicochemical properties. Real-time polymerase chain reaction assays suggest that the aragonite group can lead to higher expression of the six representative osteogenic genes, which even surpasses the amorphous calcium phosphate group and the aragonite-crystalline calcium phosphate composite group. These results illustrate that calcium carbonate and its composites with calcium phosphate are potential bone repair materials. We anticipate these mineral-based materials with controlled physiochemical properties, along with their specific fabrication techniques, can facilitate the design and production of mineral-based bone repair materials with optimized performance.

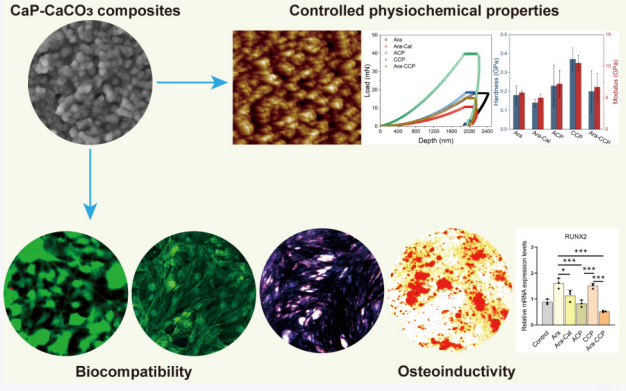

KEYWORDS: mineral-based composite films, biomimetic mineralization, calcium carbonate, calcium phosphate, bone regeneration

1 Introduction

Bone repair materials are of crucial importance for faster recovery of bone defects, especially the critical bone defects that cannot be spontaneously repaired [1]. Ideal bone grafts have to integrate several advantages, including the proper mechanical properties, the high biocompatibility, the high osteogenic capability, the tunable biodegradability, and the good accessibility [2]. Currently, autologous bone grafts are regarded as the golden standard for clinical bone regeneration. Yet the drawbacks such as the limited supply and the morbidity at donor-site notably restrict their applications [3]. Various artificial materials have thus been developed for artificial bone grafts. The high toughness of metallic materials makes them a potential candidate, but the overwhelming mechanical properties such as the relatively high hardness can cause stress shielding. Besides, the release of metal ions during the degradation process lowers their biological activity. These problems

Received: August 25, 2024; **Revised:** September 25, 2024
Accepted: September 26, 2024

✉Address correspondence to Wen-Zhi Zhang, wenzhizhang@ustc.edu.cn; Li-Bo Mao, maolb@ustc.edu.cn; Shu-Hong Yu, shyu@ustc.edu.cn

can lead to the wear and inflammation of native tissue and the restrained bone integration [4]. By comparison, bioactive ceramics have excellent biological properties but exhibit low mechanical strength and fracture toughness [5]. While some polymer materials have both good mechanical properties and high biological activity, their application are limited by the acidic products generated during their degradation, which destruct the local microenvironment around the bone defects. Specifically, polyether ether ketone (PEEK) has received increasing attention because its mechanical properties are more compatible with the human bone. Nevertheless, its biological inertness and hydrophobicity can impede bone integration, retarding its better performance for biomedical applications.

Because of their similar constituents with natural bone, mineral-based composites have long been deemed a promising candidate for bone regeneration. While these composites can show both high biocompatibility and high osteogenic capability because of their constituents. Meanwhile, their low fracture toughness has also been enhanced by biomimetic structural designs [6–8]. More importantly, minerals can have many crystalline phases as well as amorphous phases with different compositions [9, 10]. This offers great opportunities to fabricate various mineral-based composites with diverse physiochemical properties, which would substantially affect their performance for bone regeneration. Because the inorganic phase in natural bone is hydroxyapatite, which is essentially a calcium phosphate salt, the bone repair capabilities of various calcium phosphate salts have been extensively studied [11–13]. However, calcium carbonate, which is also a widespread mineral in biological materials, has received much less attention [13–16]. Nevertheless, calcium carbonate is found to be homologous to calcium phosphate in the evolution tree. Even in the hydroxyapatite of human bone, some of the phosphate ions are replaced by carbonate ions, implying the possibility of incorporating calcium carbonate in bone repair materials. Moreover, rather than using the mineral phase in graft materials directly, bone regeneration process involves the decomposition of the mineral phase and the subsequent remineralization [17–21]. In this regard, calcium carbonate, which is more chemically unstable than calcium phosphate, should also be able to play a role in bone regeneration.

Surface roughness has been reported to influence cell division, proliferation and osteogenic behavior by affecting protein adsorption, cell adhesion and cell diffusion on the material surface [22, 23]. In addition, different mineral ions, such as calcium ions, phosphate ions and carbonate ions, can affect cell adhesion and growth, by which the difference in mineral phase and ion content can lead to the difference in cell activity and osteogenic induction ability [24–26]. Therefore, it is necessary to systematically evaluate the potentials of calcium carbonate and its composites with calcium phosphate for bone regeneration applications. Owing to the tunability of biomimetic mineralization process, these physiochemical properties have been properly controlled for both calcium carbonate and calcium phosphate in previous reports [27–32]. We herein reported the fabrication of five distinct mineral-based composite films via the mineralization of calcium phosphate and calcium carbonate on chitin, which is a biopolymer with renowned advantages for biomedical applications [33]. These films were composed of different mineral phases associated with the two compounds. The physiochemical properties of these films that have been proved to affect the material performance in bone regeneration, such as their surface roughness, modulus, hardness, and degradation rate, were comparatively studied [4, 34]. The results revealed non-negligible differences between the films, indicating that the physiochemical properties of these composites could be tuned according to clinical requirements. Moreover, elaborated cell experiments demonstrated the osteogenic differentiation characteristics of these films varied from each other, although all films exhibited good biocompatibility. Notably, the aragonite group, which is a crystalline phase of calcium carbonate, and the crystalline calcium phosphate group showed the highest osteogenic gene expression, which suggested the possibility of using calcium carbonate in bone repair materials.

2 Results and discussion

2.1 Syntheses and composition analyses

The phase control of the calcium carbonate-calcium phosphate composite films was achieved by tuning the mineralization solutions, in which the chitin substrate films were mineralized (please see 4.2–4.7 in Experimental section). Specifically, high Mg^{2+} concentration led to the formation of pure aragonite (sample: Ara), whereas low Mg^{2+} ion concentration led the formation of aragonite-calcite (sample: Ara-Cal). In addition, high polyaspartic acid (PASP) concentration induced the precipitation of amorphous calcium phosphate (sample: ACP), while low PASP concentration induced crystalline calcium phosphate (sample: CCP). As carbonate substitution has been found in the hydroxyapatite of human bone, a film containing both aragonite and crystalline calcium phosphate (sample: Ara-CCP) was also synthesized via a two-step mineralization process [20, 21]. The mineral contents of these mineral-based composite films are about 70%, which were estimated through thermogravimetric analyses (Fig. S7 in the Electronic Supplementary Material (ESM)). The information of five films are summarized in Table S5 in the ESM.

Scanning electron microscopy (SEM) images showed that all the films have a continuous mineralized surface consisting of packed nanoparticles (Figs. 1(a-i)–1(e-i)). Cross-sectional images suggested the mineralization occurred not only on the surface but also inside the chitin matrix (Figs. 1(a-ii)–1(e-ii)). Elemental analyses showed the presence of Ca, C, P and O in these films, which were in line with their respective mineral phases (Figs. S1–S5 in the ESM). Notably, although there is a sequential order of growth, the mineral phase of the Ara-CCP group is homogeneous rather than heterogeneous. This can be explained by the interconversion of the calcium-based minerals via dissolution and recrystallization. To explore the crystallographic properties of the films, the samples were examined by high resolution transmission electron microscopy (HRTEM). The Ara sample showed the (111) and (032) planes of aragonite (Fig. 1(a-iii)). The Ara-Cal showed the (122) plane of aragonite and (202) plane of calcite (Fig. 1(b-iii)). While the ACP sample showed no lattice (Fig. 1(c-iii)), indicating its amorphous nature, the CCP showed the characteristic (110) plane of crystalline calcium phosphate (Fig. 1(d-iii)). Similarly, the Ara-CCP revealed both the (111) plane that is characteristic to aragonite, and the (112) plane characteristic to hydroxyapatite (Fig. 1(e-iii)). The HRTEM observations agree with the X-ray diffraction (XRD) data, except that the XRD data revealed the existence of more crystalline phases of calcium phosphate in the CCP and the Ara-CCP (Fig. S6 in the ESM). The difference can be explained by that the two characterization methods are acting on two distinct length scales.

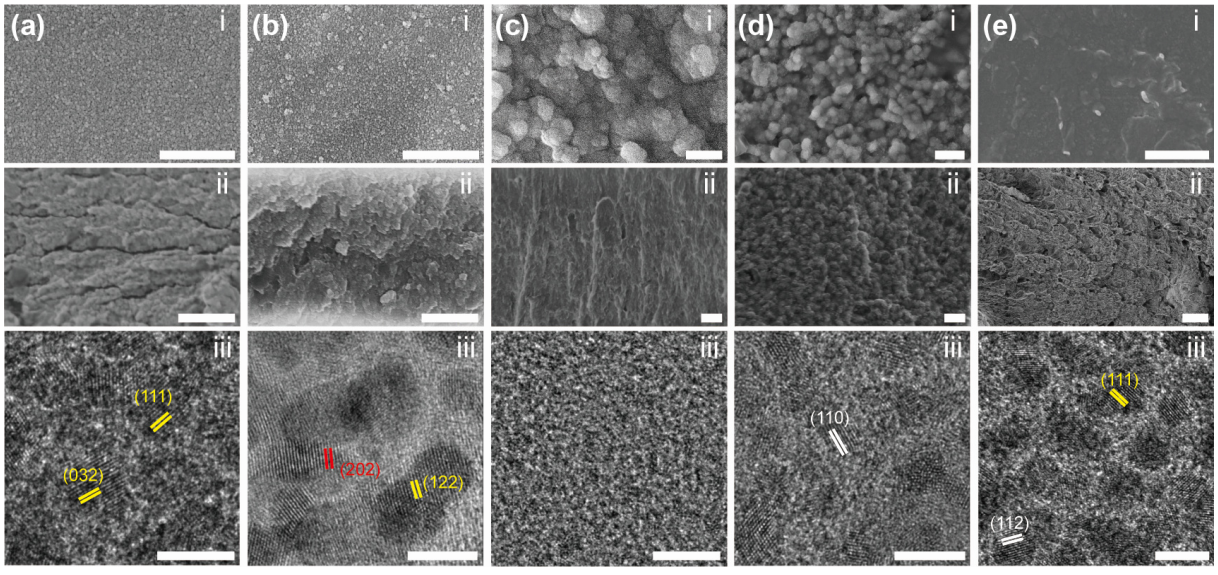

Figure 1 SEM and HRTEM micrographs of the five mineral-based films revealing their (i) surfaces, (ii) cross sections, and (iii) crystallographic features: (a) Ara; (b) Ara-Cal; (c) ACP; (d) CCP; (e) Ara-CCP. Scale bars are 1 μm for (i) and (ii), 5 nm for (iii). Notes in (iii): yellow–aragonite; red–calcite; white–hydroxyapatite.

To further verify the composition of the composite films, Fourier transform infrared spectroscopy (FTIR) analysis was performed (Fig. S8 in the ESM). The spectrum of the Ara sample showed the asymmetric aragonite CO_3^{2-} stretching vibration at 1488 cm^{-1}, the symmetric aragonite CO_3^{2-} stretching vibration at 1083 cm^{-1}, the aragonite CO_3^{2-} out-of-plane bending vibration at 858 cm^{-1}, and the split peaks at 700 and 713 cm^{-1}, which could be ascribed to the CO_3^{2-} in-plane bending vibration [35–37]. For the Ara-Cal sample, the characteristic peak at 1083 cm^{-1} could be attributed to the symmetric aragonite CO_3^{2-} stretching vibration. The calcite CO_3^{2-} asymmetric stretching vibration was responsible for the peak at 1420 cm^{-1}, whereas its out-of-plane bending absorption was represented by the peak at 873 cm^{-1} [36–38]. The FTIR also revealed the difference between the two calcium phosphate-based films. The single peak at 570 cm^{-1} in the ACP spectrum was characteristic to the PO_4^{3-} in amorphous calcium phosphate [39]. Meanwhile, the two absorption peaks at 602 and 570 cm^{-1} in the CCP spectrum could be attributed to hydroxyapatite, and the 1651 and 874 cm^{-1} to brushite [40–44]. Furthermore, in the spectrum of the Ara-CCP sample, the presence of aragonite could be proved by several peaks that could be ascribed to aragonite CO_3^{2-}: the symmetric tensile vibration at 1110 cm^{-1}, the in-plane bending vibration at 713 cm^{-1}. Besides, the peaks around 1063 cm^{-1} could be attributed to the PO_4^{3-} in hydroxyapatite, and the 1651 and 874 cm^{-1} to brushite [40–45].

We also conducted Raman spectroscopy measurements to determine the mineral composition. The peaks at 210 and 1084 cm^{-1} indicating that the presence of aragonite could be observed in the spectra of Ara, Ara-Cal and Ara-CCP samples [36, 46]. The peaks at 280, 458 and cm^{-1} attesting to the presence of calcite could be found in the Ara-Cal spectrum [46, 47]. The peaks at 430 and 960 cm^{-1} ascribed to hydroxyapatite, and the peaks at 207, 587 and 875 cm^{-1} ascribed to brushite were presented in the two samples containing crystalline calcium phosphate [42, 43, 45, 48–50]. Nevertheless, the peak characteristic to amorphous calcium phosphate were weaker than those for crystalline calcium phosphate and shifted to 952 cm^{-1} (Fig. S9 in the ESM) [48]. Therefore, both the FTIR and the Raman spectroscopy further validate the mineral composition of the five composite films.

2.2 Surface morphological and mechanical properties

Because the material surface morphology and mechanical properties strongly affect its performance both *in vitro* and *in vivo*, microscale surface analyses of the five films were conducted to study if the presence of calcium carbonate could endow the mineral-based materials with new bone repair potentials. Atomic force microscopy (AFM) revealed the nanoparticulated surfaces of all the films (Figs. 2(a)–2(e)). The surface roughness of each composite film was compared through height analysis (Fig. 2(f)). The result suggested that, while the surface height of the other groups did not deviate too much from the average value, that of the Ara-CCP sample fluctuated notably, indicating this film had a relatively rough surface. The results were consistent with the arithmetic mean roughness Ra and the height distribution of the AFM images (Figs. 2(a)–2(e), and 2(g)). The different surface roughness of these film materials might lead to different cell attachment, growth and migration during bone regeneration process.

The microscale mechanical properties of the films were analyzed by means of nanoindentation tests (Figs. 2(h)–2(i)). In the depth-control mode, the CCP sample required the largest load to achieve a given depth, whereas the Ara-Cal required the smallest load at the fixed depth (Fig. 2(h)). The required loads for the other three samples were similar, but were much smaller than that of the CCP. A possible explanation for the results is the different crystallinity and the packing density of the samples. Accordingly, the CCP sample exhibited the highest hardness and modulus, while the Ara-Cal showed the lowest (Fig. 2(i)). As it has been reported that the mechanical properties of bone graft materials are key to the osseointegration, such tunable hardness and modulus caused by the incorporation of calcium carbonate and the phase-controlled mineralization would be beneficial for optimizing the *in vivo* performance of bone graft materials [51].

2.3 *In vitro* biocompatibility and degradation behavior

To ensure the applicability of these mineral-based materials either

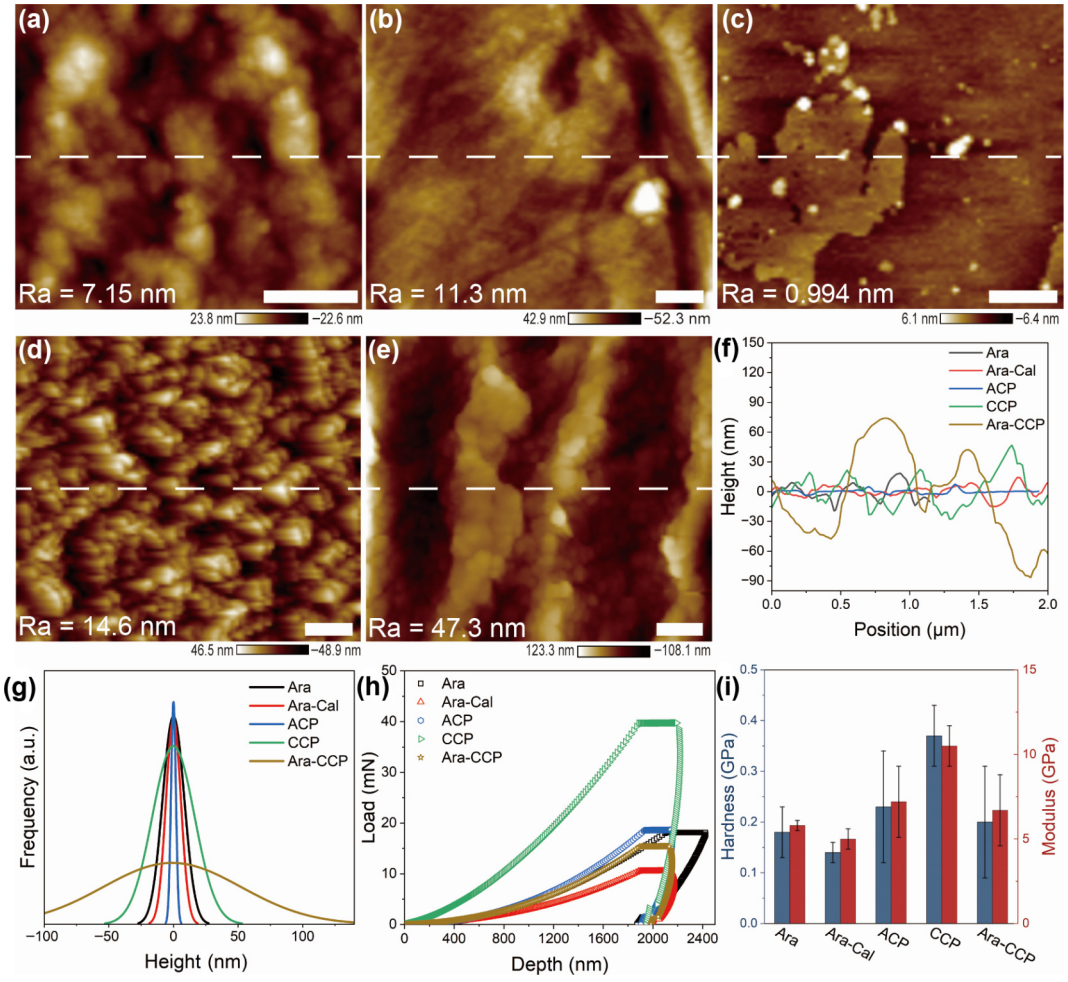

Figure 2 Microscopic surface roughness and mechanical properties. Surface morphologies of (a) Ara, (b) Ara-Cal, (c) ACP, (d) CCP, and (e) Ara-CCP. Arithmetic mean roughness (Ra) was at the bottom left of each graph. (f) Surface profile along the dashed lines in each graph. (g) Height distribution derived from (f). (h) Nano indentation-based load-displacement curves of each sample. (i) Hardness and modulus of the samples calculated from nano indentation data. Scale bars are 300 nm for (a)–(e).

in the form of film or bulk for tissue engineering, their *in vitro* biocompatibility and degradation behavior were evaluated. To verify the biocompatibility of the materials, especially those with calcium carbonate incorporation, MC3T3-E1 cells (murine calvarial osteoblast cell line) were co-cultured with the five sample groups and blank control group respectively. The cell biocompatibility was quantitatively evaluated via cell counting kit-8 (CCK-8) assay, where the absorbance is proportional to the cell viability and thus reflects the cytotoxicity. The cell viability was measured at 24, 48 and 72 h after incubation (Figs. 3(a)–3(c)). After 24 h of culture, the cell viabilities of all the sample groups were relatively high, among which the CCP group showed the highest value. With increased incubation time, the cell viability decreased slightly compared with the control group yet remained a high level, confirming the non-cytotoxicity of these mineral-based materials.

Live/dead staining assay was also carried out on the MC3T3-E1 cells that were co-cultured with the materials. The stained cells were observed by confocal fluorescence microscopy to determine the influence of different materials on the cells. After 24 and 48 h of co-culture, almost all the MC3T3-E1 cells were alive, showing green fluorescence in the images (Figs. S10 and S11 in the ESM). In contrast, there were only a few dead cells that showed red fluorescence (marked by white circles) for all the sample groups. Even after 72 h of co-culture, living cells remained dominating (Figs. 3(d)–3(h) and Fig. S12 in the ESM). To observe the morphology and cytoskeleton structure of the co-cultured MC3T3-E1 cells, the cells were stained by Actin-Tracker Green-488 and 4',6-diamidino-2-phenylindole (DAPI) respectively. For all the sample groups with an incubation time of 24, 48 and 72 h, the cells all exhibited shuttle shapes and spread extensively (Figs. S13–S15 in the ESM). The above results thus demonstrated the good biocompatibility of all these mineral-based materials.

The proper degradation rate of bone graft materials can ensure the fast bone regeneration at the early stage of implantation and the gradual replacement of the grafts by newly formed autonomous bone, and thus is crucial for efficient bone regeneration. Considering their diverse chemical stabilities, the incorporated calcium carbonate components with controlled phases are supposed to substantially change the degradation behavior of the mineral-based films. We therefore quantitatively assessed the degradation kinetics of these materials by soaking them in phosphate-buffered saline (PBS) solution for up to 45 days (Fig. S16 in the ESM). The five sample groups showed distinct degradation curves. The residual masses gradually decreased over time, indicating a degradation tendency. The materials degraded relatively fast in the first 15 days. While the masses of the other four samples fluctuated slightly thereafter, which could be attributed to the re-deposition of the solved calcium ions minerals, the ACP

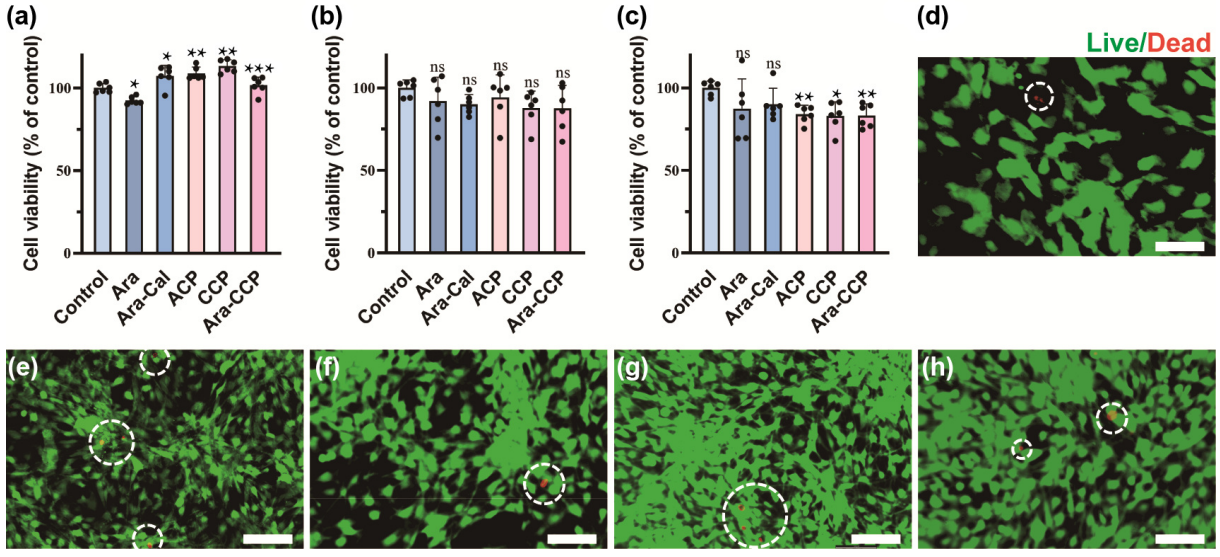

Figure 3 Viability histogram of MC3T3-E1 cells co-cultured with different materials for (a) 24 h, (b) 48 h and (c) 72 h. The data are presented as mean ± SD. Three biologically independent specimens were tested for each material. The results were analyzed via one-way ANOVA to study if the sample groups differed from the control group (ns indicates no significant difference; $^{*}P < 0.05$; $^{**}P < 0.01$; $^{***}P < 0.001$). The live/dead staining of the cells co-cultured for 72 h with (d) Ara, (e) Ara-Cal, (f) ACP, (g) CCP, and (h) Ara-CCP. The red fluorescent areas are marked with white circles (enlarged details are shown in Fig. S12 in the ESM). Scale bars: 100 μm.

sample degraded increasingly fast after 21 days. The different degradation kinetics suggested a possible difference in their osteoinduction capabilities.

2.4 *In vitro* osteoinductivity assessment

Alkaline phosphatase (ALP) is one of the functional genes expressed in the early osteogenesis process and is therefore widely used as an early osteoblast marker [41]. To evaluate the osteogenic capability of these materials, ALP activity tests were carried out. MC3T3-E1 cells were co-cultured with the sample groups for 14 and 21 days, followed by ALP staining. Optical microscopy images showed that all the sample groups were stained heavily with blue-purple color, and the density increased as the cell co-culture time elongated (Fig. 4 and Fig. S17 in the ESM). The quantitative results suggested that the ALP activities of all the sample groups were significantly higher than the control group, indicating that these mineral-based materials can effectively promote osteogenic differentiation of MC3T3-E1 cells (Fig. S18 in the ESM). In addition, among the five sample groups, the Ara and the CCP samples showed the highest ALP activities, which implied that their osteogenic differentiation capabilities were not the same.

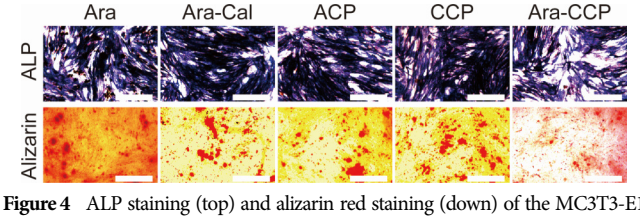

Figure 4 ALP staining (top) and alizarin red staining (down) of the MC3T3-E1 cells co-cultured with different materials after 21 days of osteogenic induction. Scale bars: 400 μm.

Calcium nodules are one of the important signs of the late stage of osteogenic differentiation [52]. The calcium nodules were observed by alizarin red staining after 14 and 21 days of co-culture of the MC3T3-E1 cells with the materials (Fig. 4 and Fig. S19 in the ESM). Calcium nodules were observed in all the material groups at both time points, and the calcium nodule number increased as the co-culture time increased. The quantitative results showed that the number of calcium nodules in all the sample groups were significantly higher than the control group, and the number of calcium nodules in Ara and CCP samples were the highest, which was in line with the ALP staining assay (Figs. S19 and S20 in the ESM). The results indicated that all these mineral-based materials had the potential to induce bone formation.

To further investigate the osteogenic performance of these mineral-based film materials, the expressions of early osteogenic markers runt-related transcription factor 2 (RUNX2), alkaline phosphatase (ALP), osterix (OSX), and osteopontin (OPN), and late osteogenic markers osteocalcin (OCN) and type I collagen (COL-I) were analyzed via real-time quantitative polymerase chain reaction (RT-qPCR) assay (Fig. 5 and Figs. S21–S23 in the ESM) [52]. Generally, the sample groups showed an enhanced osteogenic gene expression compared with the control group (Figs. S21 and S22 in the ESM). The Ara and the CCP group exhibited relatively higher expression levels of all the six markers either after 14 days or after 21 days of co-culture than the other three groups, although some of the differences were not significant. Specifically, the superiority of the Ara and the CCP groups was more pronounced in the expressions of OSX, OPN and OCN after 14 days of co-culture, whereas superiority was more pronounced for RUNX2, ALP, OSX and OCN after 21 days (Fig. 5 and Fig. S23 in the ESM). Therefore, the incorporation of calcium carbonate indeed altered the osteogenic behaviors of the mineral-based materials. The high performance of the Ara group, which was similar with that of the CCP group, also suggested its potentials for the construction of bone repair materials. Because the expressions of these markers were strongly influenced by the microenvironments in which the cells lived, the above differences could be attributed to the different microenvironments created by the degradation of these materials (Fig. S16 and Table S4 in the ESM), which were associated with the mineral compositions, phases and surface morphologies.

2.5 Discussion

Calcium phosphate and calcium carbonate have been the two main minerals used by organisms to construct their bones and

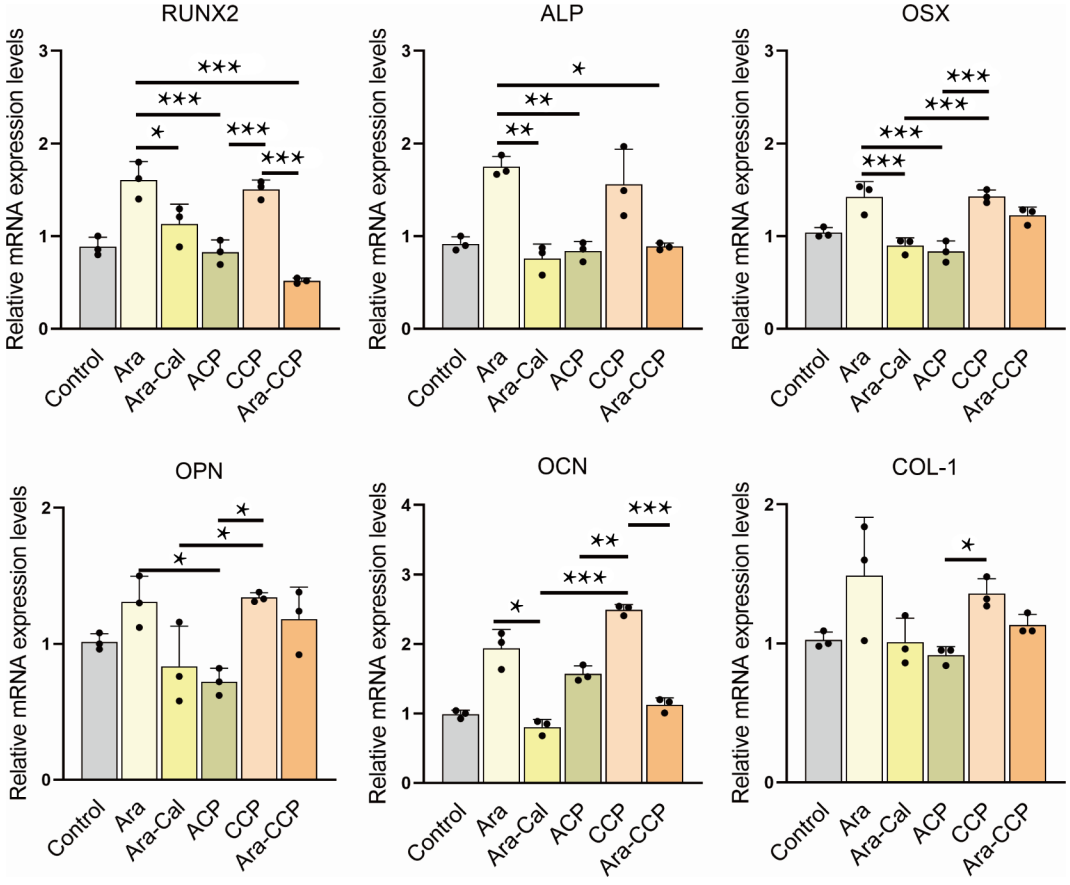

Figure 5 RT-qPCR assay of six representative osteogenesis genes (RUNX2, ALP, OSX, OPN, OCN and COL-1) after 21 days of co-culture. The data are presented as mean ± SD. The results were analyzed via one-way ANOVA (ns indicates no significant difference; $^{*}P < 0.05$; $^{**}P < 0.01$; $^{***}P < 0.001$).

exoskeletons for millions of years. Organisms develop their own calcified tissue simply by choosing specific mineral phases and adjusting the ratio of phosphate/carbonate according to the environments they live in. The two minerals also co-exist in many organisms. These facts make them essentially biologically homologous [17, 18]. Moreover, the chemical stability of calcium carbonates differs from that of calcium phosphate, by which the degradation kinetics as well as the eventual bone repair performance can be tuned. It is thus supposed that calcium carbonates can also be preferred mineral materials for the repair of bone, where hydroxyapatite is the dominate mineral phase. The *in vitro* experiments have proved the biocompatibility of the calcium carbonate-calcium phosphate composite films, and their degradation could be tuned by controlling the mineral compositions, phases and surface morphologies. Accordingly, they also exhibited osteogenic behaviors. Therefore, the design of this work is well supported by the experimental results.

3 Conclusions

In summary, we reported the fabrication of five calcium carbonate-calcium phosphate composite films with controlled compositions and phases via biomimetic mineralization. These films had different surface morphologies and mechanical properties. The incorporation of calcium carbonate did not affect the high biocompatibility of the materials; on the contrary, calcium carbonate can effectively change the degradation kinetics and the osteoinductivity of the materials. As calcium carbonate has many crystalline and amorphous phases, the results in this work provided new possibilities for designing mineral-based bone grafts [9, 10]. We thus anticipate that our findings facilitate the development of customized bone repair materials.

4 Methods

4.1 Materials

Polyacrylic acid (PAA; M_W = 1800 g·mol^{-1}) was purchased from Sigma-Aldrich, Inc. Chitosan, NaCl, $CaCO_3$, $MgCl_2{\cdot}6H_2O$, HCl, NaOH, $NaHCO_3$, acetic acid, acetic anhydride, methanol, and ethanol were purchased from Sinopharm Chemical Reagent Co., Ltd. Phosphate-buffered saline solution (PBS solution; calcium and magnesium free; pH = 7.4) was purchased from BioDee Biotechnology Co., Ltd., and was used for preparing the mineralization solution of the ACP films. PBS solution (pH = 7.4) was bought from Servicebio Technology Co., Ltd., and was used for degradation analyses. Na_2HPO_4 and $CaCl_2$ solution (1 M) were purchased from Aladdin Reagent Co., Ltd. Polyaspartic acid (PASP; M_W = 12,546 g·mol^{-1}; courtesy of Prof. Hui Cao from Beijing University of Chemical Technology). Tris-HCl solution (1 M; pH = 9.0) was acquired from Sangon Biotech Co., Ltd. Lysozyme (activity ≥ 20,000 units/mg) was bought form Labgic Technology Co., Ltd. All reagents were used as received without further purification.

4.2 Preparation of chitin substrate film

2 wt.% chitosan aqueous solution was prepared by adding 2 g of

chitosan powder into 96 mL of de-ionized water (DIW), and then 2 mL of acetic acid was added dropwise into the suspension under vigorous stirring. 10 mL of the above chitosan solution was evenly spread in a circular petri dish with a diameter of 10 cm and dried in an oven at 60 °C. The dried chitosan films were treated with a mixed solution of methanol and acetic anhydride (volume ratio was 10 to 1) at 50 °C for 4 h to convert chitosan film into chitin substrate films, which was quite stable in aqueous solution.

4.3 Preparation of Ara film

$CaCO_3$ suspension was bubbled with CO_2 under vigorous stirring at 25 °C for 4 h to obtain saturated $CaHCO_3$ solution. The residual $CaCO_3$ was filtered to obtain a clear $CaHCO_3$ solution, where the Ca^{2+} concentration was approximately 10 mM. PAA and Mg^{2+} were used as additives to control the phase of the mineralization products. Specifically, the mineralization of Ara film material was induced by adding 0.3 mL of PAA solution (0.2 M) and 6 mL of $MgCl_2$ solution (2 M) to 100 mL of the above $CaHCO_3$ solution. A prepared chitin film (2 cm × 2 cm) were immersed into this mineralization solution, which was then placed in an oven at 42 °C for two days. The obtained mineralized film was thoroughly rinsed with DIW.

4.4 Preparation of Ara-Cal film

The procedures were similar with the preparation of Ara film except for the amount of the additives. The mineralization solution was obtained by adding 0.1 mL of PAA and 0.2 mL of $MgCl_2$ to 100 mL of the above saturated $CaHCO_3$ solution.

4.5 Preparation of ACP film

A modified simulated body fluid (SBF) was prepared first as mineralization solution (Table S1 in the ESM). A chitin film was immersed into 100 mL of the SBF solution and placed in an oven at 37 °C for 3 days. The obtained mineralized film was thoroughly rinsed with DIW.

4.6 Preparation of CCP film

The SBF was further modified for the preparation of CCP film (Table S2 in the ESM). The chitin film mineralization was kept at 45 °C for five days. To further improve the crystallinity, the mineralized films were placed in DIW at 60 °C for 1 day.

4.7 Preparation of Ara-CCP film

A chitin film was mineralized with the CCP mineralization solution and then the Ara mineralization solution successively. The procedures were the same as those described above.

4.8 Characterizations

Scanning electron microscopy (SEM) characterization was carried out on a Zeiss Gemini450 scanning electron microscope equipped with an Oxford ULTIM MAX100 detector. HRTEM characterization was performed on an FEI Talos F200X transmission electron microscope. An ultrathin cross-sectional slice of the film used for HRTEM observation was obtained by focused ion beam (FIB) technique. FTIR spectroscopy was acquired with a Thermo Nicolet iN10 Fourier transform infrared spectrophotometer. Thermogravimetric analyses (TGA) were operated using a TA Instruments TGA Q5000IR thermogravimetric analyzer. X-ray diffraction (XRD) data were acquired with a Philips X'Pert 1 X-ray diffractometer. Raman spectroscopy data were obtained by a LabRAM Confocal Raman spectrometer equipped with a 785 nm excitation laser. Inductively coupled plasma optic emission spectroscopy (ICP-OES) was performed on a PerkinElmer Avio 220 MAX ICP-OES. AFM images were obtained via a Bruker Dimension Icon atomic force microscope under the tapping mode. Nanoindentation tests were carried out using a Bruker Hysitron TI 980 nanoindenter equipped with a triangular pyramid (Berkovich) tip. Each sample was tested at least five times.

4.9 *In vitro* degradation test

Six parallel specimens at each time point were prepared for each of the five film materials. Each sample initially weighed ~ 0.025 g, and the precise mass was noted as W_1. The degradation solution was prepared by mixing lysozyme (final concentration was 0.1 g·L^{-1}) and 25 mL of PBS solution. Specimens were immersed in the above degradation solution and placed in a shaker at 37 °C. The dry weight (W_2) was measured and recorded after 1, 3, 7, 14, 21, 30, and 45 days respectively. The degradation rate R_d for each specimen at each time point was then calculated by Eq. (1)

$$R_d = \frac{W_1 - W_2}{W_1} \times 100\% \quad (1)$$

4.10 Cytological experiment

4.10.1 Acquisition of material extracts

Aqueous extracts of the film materials were used for cytological experiments (control group: blank, i.e., no material was used). The extracts were obtained according to the ISO10993-12 standard. For cell activity assays, the extraction medium was α-MEM medium solution (Gibco) containing fetal bovine serum (0.1 mL·mL^{-1}), penicillin (100 U·mL^{-1}) and streptomycin (100 mg·mL^{-1}) (Gibco). The disinfected material was put into a sterilized culture bottle, and the extraction medium was added (the ratio of the material to the extraction medium was 0.1 g per 1 mL, which was about 6 cm^2 of the film per 1 mL of medium). Then they were co-incubated for 72 h (37 °C, 95% relative humidity, and 5% CO_2) to obtain the material extracts. For osteogenic assays, the extraction medium was osteogenic induction medium (MUXMT-90021). All extracts were stored at 4 °C for subsequent experiments. The Ca^{2+} concentration in the extracts as well as in the media was measured by ICP-OES, and three independent tests were carried out for each sample.

4.10.2 Live/dead staining test

The culture medium of MC3T3-E1 cells was replaced by the above material extracts (α-MEM medium). Observation and detection of cell viability were accomplished using the LIVE/DEAD™ Viability/Cytotoxicity Kit (Invitrogen). The staining was carried out by incubation at room temperature for 45 min. The cells were then observed using a fluorescence microscope (Olympus IX51). The percentages of living and dead cells were analyzed statistically.

4.10.3 Cell skeletal staining test

The culture medium of MC3T3-E1 cells was replaced by the above material extracts (α-MEM medium). The cells were fixed and stained with Actin-Tracker Green-488 and 4',6-diamidino-2-phenylindole (DAPI; Beyotime Biotechnology) and Actin-Tracker Green-488 dye (Beyotime Biotechnology). Each staining lasted for 5 min. The cells were rinsed by soaking in PBS solution 3 times,

and each time lasted for 5 min to remove the remaining staining solution.

4.10.4 CCK-8 assay

The culture medium of MC3T3-E1 cells was replaced by the above material extracts (α-MEM medium). Cell counting kit-8 (CCK-8; 7Sea Biotech) was used for detection. The optical density (OD) values at 450 nm were measured by an enzyme-linked immunosorbent assay (ELISA) microplate reader and analyzed statistically. The cell viability was calculated using Eq. (2)

$$\text{Cell viability} = \frac{OD_e - OD_b}{OD_c - OD_b} \times 100\% \quad (2)$$

where OD_e was the optical density of the experimental groups, OD_b was the optical density of the blank group (cell free), and OD_c was the optical density of the control group.

4.10.5 Alizarin red staining test

24-well plates were pretreated with 0.1% gelatin (Beyotime Biotechnology). The MC3T3-E1 cells were seeded in the above plates at a density of 2×10^4 cells/well. After 24 h of culture, the original culture medium was replaced by the above material extracts (osteogenic induction medium). The medium was renewed every 2 days, and the calcium nodules were observed via staining with alizarin red staining solution (Cyagen Biosciences). After the observation, 10% cetylpyridine chloride was added to dissolve calcium nodules for 30 min, and OD value at 570 nm was determined by enzymoleter for statistical analysis.

4.10.6 ALP staining and analysis

The procedures of the alkaline phosphatase (ALP) staining were similar with the alizarin red staining except that the staining solution was ALP solution (Beyotime Biotechnology). The quantitative analysis of ALP activity was performed using Alkaline Phosphatase Assay Kit (Beyotime Biotechnology).

4.10.7 RT-qPCR assay

The cell culture procedures were similar with those of the alizarin red staining test. After 14 and 21 days of culture, RT-qPCR technique was used to examine the expression of osteogenic differentiation gene markers, including RUNX2, ALP, OSX, OPN, OCN and COL-I. The GAPDH was used as an internal reference, and the data were statistically analyzed according to $2^{-\Delta\Delta CT}$. The primer sequences were shown in Table S3 in the ESM.

4.10.8 Statistical analysis

All data are expressed as mean ± standard deviation (SD). One-way analysis of variance (ANOVA) was used for statistical analysis of comparisons between multiple data groups. $P < 0.05$ was considered statistically significant: $^*P < 0.05$; $^*P < 0.01$; $^{***}P < 0.001$.

Electronic Supplementary Material: Supplementary material (elemental mapping, XRD, TGA, FTIR, Raman, cell staining, and RT-qPCR) is available in the online version of this article at https://doi.org/10.26599/NR.2025.94907055.

Data availability

All data needed to support the conclusions in the paper are presented in the manuscript and/or the Electronic Supplementary Material. Additional data related to this paper may be requested from the corresponding author upon request.

Acknowledgements

This work was supported by the Strategic Priority Research Program of the Chinese Academy of Sciences (No. XDB047030306), the National Key Research and Development Program of China (Nos. 2018YFE0202201 and 2021YFA0715700), the National Natural Science Foundation of China (Nos. 22293044 and 22422507), and the New Cornerstone Investigator Program. This work was partially carried out at the USTC Center for Micro and Nanoscale Research and Fabrication.

Declaration of competing interest

All the contributing authors report no conflict of interests in this work. Author Shu-Hong Yu is the editorial board member of this journal, but he is not involved in the peer review or decision of this article.

Author contribution statement

Y.-L. Y.: Data curation, validation, writing – original draft, experimental design. X.-W. G.: Data curation, validation, experimental design. Y.-F. M.: Data curation. W.-Z. Z.: Project administration, funding acquisition. L.-B. M.: Conceptualization, project administration, funding acquisition, writing – review & editing. S.-H. Y.: Conceptualization, project administration, funding acquisition, writing – review & editing. All the authors have approved the final manuscript.

Informed consent

Not applicable.

Ethics statement

Not applicable.

Use of AI statement

None.

References

[1] Koons, G. L.; Diba, M.; Mikos, A. G. Materials design for bone-tissue engineering. *Nat. Rev. Mater.* **2020**, *5*, 584–603.
[2] Haugen, H. J.; Lyngstadaas, S. P.; Rossi, F.; Perale, G. Bone grafts: Which is the ideal biomaterial. *J. Clin. Periodontol.* **2019**, *46*, 92–102.
[3] Schmidt, A. H. Autologous bone graft: Is it still the gold standard. *Injury* **2021**, *52*, S18–S22.
[4] Prasad, K.; Bazaka, O.; Chua, M.; Rochford, M.; Fedrick, L.; Spoor, J.; Symes, R.; Tieppo, M.; Collins, C.; Cao, A. et al. Metallic biomaterials: Current challenges and opportunities. *Materials* **2017**, *10*, 884.
[5] Kaur, G.; Kumar, V.; Baino, F.; Mauro, J. C.; Pickrell, G.; Evans, I.; Bretcanu, O. Mechanical properties of bioactive glasses, ceramics, glass-ceramics and composites: State-of-the-art review and future challenges. *Mater. Sci. Eng. C* **2019**, *104*, 109895.
[6] Meng, Y. F.; Yu, C. X.; Zhou, L. C.; Shang, L. M.; Yang, B.; Wang, Q. Y.; Meng, X. S.; Mao, L. B.; Yu, S. H. Nanograded artificial nacre with efficient energy dissipation. *Innovation* **2023**, *4*, 100505.
[7] Xiao, C. L.; Li, M.; Wang, B. J.; Liu, M. F.; Shao, C. Y.; Pan, H. H.;

Lu, Y.; Xu, B. B.; Li, S. W.; Zhan, D. et al. Total morphosynthesis of biomimetic prismatic-type $CaCO_3$ thin films. *Nat. Commun.* **2017**, *8*, 1398.

[8] Meng, Y. F.; Zhu, Y. B.; Zhou, L. C.; Meng, X. S.; Yang, Y. L.; Zhao, R.; Xia, J.; Yang, B.; Lu, Y. J.; Wu, H. A. et al. Artificial nacre with high toughness amplification factor: Residual stress-engineering sparks enhanced extrinsic toughening mechanisms. *Adv. Mater.* **2022**, *34*, 2108267.

[9] Zou, Z. Y.; Habraken, W. J. E. M.; Matveeva, G.; Jensen, A. C. S.; Bertinetti, L.; Hood, M. A.; Sun, C. Y.; Gilbert, P. U. P. A.; Polishchuk, I.; Pokroy, B. et al. A hydrated crystalline calcium carbonate phase: Calcium carbonate hemihydrate. *Science* **2019**, *363*, 396–400.

[10] Sun, S. T.; Mao, L. B.; Lei, Z. Y.; Yu, S. H.; Cölfen, H. Hydrogels from amorphous calcium carbonate and polyacrylic acid: Bio-inspired materials for "mineral plastics". *Angew. Chem., Int. Ed.* **2016**, *55*, 11765–11769.

[11] Chen, S.; Liu, D. C.; Fu, L.; Ni, B.; Chen, Z. K.; Knaus, J.; Sturm, E. V.; Wang, B. H.; Haugen, H. J.; Yan, H. J. et al. Formation of amorphous iron-calcium phosphate with high stability. *Adv. Mater.* **2023**, *35*, 2301422.

[12] Chen, S.; Krumova, M.; Cölfen, H.; Sturm, E. V. Synthesis of fiber-like monetite without organic additives and its transformation to hydroxyapatite. *Chem. Mater.* **2019**, *31*, 1543–1551.

[13] Meyers, M. A.; McKittrick, J.; Chen, P. Y. Structural biological materials: Critical mechanics-materials connections. *Science* **2013**, *339*, 773–779.

[14] Meyers, M. A.; Chen, P. Y.; Lin, A. Y. M.; Seki, Y. Biological materials: Structure and mechanical properties. *Prog. Mater. Sci.* **2008**, *53*, 1–206.

[15] Liu, Z. M.; Shao, C. Y.; Jin, B.; Zhang, Z. S.; Zhao, Y. Q.; Xu, X. R.; Tang, R. K. Crosslinking ionic oligomers as conformable precursors to calcium carbonate. *Nature* **2019**, *574*, 394–398.

[16] Meng, X. S.; Zhou, L. C.; Liu, L.; Zhu, Y. B.; Meng, Y. F.; Zheng, D. C.; Yang, B.; Rao, Q. Z.; Mao, L. B.; Wu, H. A. et al. Deformable hard tissue with high fatigue resistance in the hinge of bivalve *Cristaria plicata*. *Science* **2023**, *380*, 1252–1257.

[17] Ajili, W.; Tovani, C. B.; Fouassier, J.; de Frutos, M.; Laurent, G. P.; Bertani, P.; Djediat, C.; Marin, F.; Auzoux-Bordenave, S.; Azaïs, T. et al. Inorganic phosphate in growing calcium carbonate abalone shell suggests a shared mineral ancestral precursor. *Nat. Commun.* **2022**, *13*, 1496.

[18] Bentov, S.; Aflalo, E. D.; Tynyakov, J.; Glazer, L.; Sagi, A. Calcium phosphate mineralization is widely applied in crustacean mandibles. *Sci. Rep.* **2016**, *6*, 22118.

[19] Reznikov, N.; Bilton, M.; Lari, L.; Stevens, M. M.; Kröger, R. Fractal-like hierarchical organization of bone begins at the nanoscale. *Science* **2018**, *360*, eaao2189.

[20] Boskey, A. L.; Robey, P. G. The composition of bone. In *Primer on the Metabolic Bone Diseases and Disorders of Mineral Metabolism*; 9th ed. Bilezikian, J. P.; Bouillon, R.; Clemens, T.; Compston, J.; Bauer, D. C.; Ebeling, P. R.; Engelke, K.; Goltzman, D.; Guise, T.; Jan de Beur, S. M. et al., Eds.; Wiley-Blackwell: Hoboken, 2019; pp 84–92.

[21] Von Euw, S.; Wang, Y.; Laurent, G.; Drouet, C.; Babonneau, F.; Nassif, N.; Azaïs, T. Bone mineral: New insights into its chemical composition. *Sci. Rep.* **2019**, *9*, 8456.

[22] Santander-Borrego, M.; Taran, E.; Shadforth, A. M. A.; Whittaker, A. K.; Chirila, T. V.; Blakey, I. Hydrogels with Lotus Leaf Topography: Investigating surface properties and cell adhesion. *Langmuir* **2017**, *33*, 485–493.

[23] Ermis, M.; Antmen, E.; Hasirci, V. Micro and Nanofabrication methods to control cell-substrate interactions and cell behavior: A review from the tissue engineering perspective. *Bioact. Mater.* **2018**, *3*, 355–369.

[24] Maeno, S.; Niki, Y.; Matsumoto, H.; Morioka, H.; Yatabe, T.; Funayama, A.; Toyama, Y.; Taguchi, T.; Tanaka, J. The effect of calcium ion concentration on osteoblast viability, proliferation and differentiation in monolayer and 3D culture. *Biomaterials* **2005**, *26*, 4847–4855.

[25] Salam, N.; Gibson, I. R. Lithium ion doped carbonated hydroxyapatite compositions: Synthesis, physicochemical characterisation and effect on osteogenic response *in vitro*. *Biomater. Adv.* **2022**, *140*, 213068.

[26] Kim, H. D.; Jang, H. L.; Ahn, H. Y.; Lee, H. K.; Park, J.; Lee, E. S.; Lee, E. A.; Jeong, Y. H.; Kim, D. G.; Nam, K. T. et al. Biomimetic whitlockite inorganic nanoparticles-mediated *in situ* remodeling and rapid bone regeneration. *Biomaterials* **2017**, *112*, 31–43.

[27] Yamamoto, Y.; Nishimura, T.; Saito, T.; Kato, T. $CaCO_3$/chitin-whisker hybrids: formation of $CaCO_3$ crystals in chitin-based liquid-crystalline suspension. *Polym. J.* **2010**, *42*, 583–586.

[28] Matsumura, S.; Kajiyama, S.; Nishimura, T.; Kato, T. Formation of helically structured chitin/$CaCO_3$ hybrids through an approach inspired by the biomineralization processes of crustacean cuticles. *Small* **2015**, *11*, 5127–5133.

[29] Zhu, F. J.; Nishimura, T.; Eimura, H.; Kato, T. Supramolecular effects on formation of $CaCO_3$ thin films on a polymer matrix. *CrystEngComm* **2014**, *16*, 1496–1501.

[30] Zhu, F. J.; Nishimura, T.; Sakamoto, T.; Tomono, H.; Nada, H.; Okumura, Y.; Kikuchi, H.; Kato, T. Tuning the stability of $CaCO_3$ crystals with magnesium ions for the formation of aragonite thin films on organic polymer templates. *Chem. Asian J.* **2013**, *8*, 3002–3009.

[31] Kajiyama, S.; Sakamoto, T.; Inoue, M.; Nishimura, T.; Yokoi, T.; Ohtsuki, C.; Kato, T. Rapid and topotactic transformation from octacalcium phosphate to hydroxyapatite (HAP): A new approach to self-organization of free-standing thin-film HAP-based nanohybrids. *CrystEngComm* **2016**, *18*, 8388–8395.

[32] Nakayama, M.; Kajiyama, S.; Kumamoto, A.; Nishimura, T.; Ikuhara, Y.; Yamato, M.; Kato, T. Stimuli-responsive hydroxyapatite liquid crystal with macroscopically controllable ordering and magneto-optical functions. *Nat. Commun.* **2018**, *9*, 568.

[33] Cheung, R. C. F.; Ng, T. B.; Wong, J. H.; Chan, W. Y. Chitosan: An update on potential biomedical and pharmaceutical applications. *Mar. Drugs* **2015**, *13*, 5156–5186.

[34] Sadtler, K.; Singh, A.; Wolf, M. T.; Wang, X. K.; Pardoll, D. M.; Elisseeff, J. H. Design, clinical translation and immunological response of biomaterials in regenerative medicine. *Nat. Rev. Mater.* **2016**, *1*, 16040.

[35] Xyla, A. G.; Koutsoukos, P. G. Quantitative analysis of calcium carbonate polymorphs by infrared spectroscopy. *J. Chem. Soc. Faraday Trans. 1* **1989**, *85*, 3165–3172.

[36] Chakrabarty, D.; Mahapatra, S. Aragonite crystals with unconventional morphologies. *J. Mater. Chem.* **1999**, *9*, 2953–2957.

[37] Loftus, E.; Rogers, K.; Lee-Thorp, J. A simple method to establish calcite: Aragonite ratios in archaeological mollusc shells. *J. Quat. Sci.* **2015**, *30*, 731–735.

[38] Wada, N.; Horiuchi, N.; Nakamura, M.; Nozaki, K.; Nagai, A.; Yamashita, K. Controlled crystallization of calcium carbonate via cooperation of polyaspartic acid and polylysine under double-diffusion conditions in agar hydrogels. *ACS Omega* **2018**, *3*, 16681–16692.

[39] Indurkar, A.; Choudhary, R.; Rubenis, K.; Nimbalkar, M.; Sarakovskis, A.; Boccaccini, A. R.; Locs, J. Amorphous calcium phosphate and amorphous calcium phosphate carboxylate: Synthesis and characterization. *ACS Omega* **2023**, *8*, 26782–26792.

[40] Wei, W.; Lei, Y.; Zhong, W.; Cui, J.; Wei, Z. Mechanism of enhanced humic acid removal from aqueous solution using poorly crystalline hydroxyapatite nanoparticles. *Dig. J. Nanomater. Biostruct.* **2015**, *10*, 663–680.

[41] Rapacz-Kmita, A.; Ślósarczyk, A.; Paszkiewicz, Z.; Paluszkiewicz, C. Phase stability of hydroxyapatite-zirconia (HAp–ZrO_2) composites for bone replacement. *J. Mol. Struct.* **2004**, *704*, 333–340.

[42] Antonakos, A.; Liarokapis, E.; Leventouri, T. Micro-Raman and FTIR

studies of synthetic and natural apatites. *Biomaterials* **2007**, *28*, 3043–3054.
[43] Xu, J. W.; Butler, I. S.; Gilson, D. F. R. FT-Raman and high-pressure infrared spectroscopic studies of dicalcium phosphate dihydrate ($CaHPO_4·2H_2O$) and anhydrous dicalcium phosphate ($CaHPO_4$). *Spectrochim. Acta Part A* **1999**, *55*, 2801–2809.
[44] Boanini, E.; Silingardi, F.; Gazzano, M.; Bigi, A. Synthesis and hydrolysis of brushite (DCPD): The role of ionic substitution. *Cryst. Growth Des.* **2021**, *21*, 1689–1697.
[45] Karampas, I. A.; Kontoyannis, C. G. Characterization of calcium phosphates mixtures. *Vib. Spectrosc.* **2013**, *64*, 126–133.
[46] Kontoyannis, C. G.; Vagenas, N. V. Calcium carbonate phase analysis using XRD and FT-Raman spectroscopy. *Analyst* **2000**, *125*, 251–255.
[47] Behrens, G.; Kuhn, L. T.; Ubic, R.; Heuer, A. H. Raman spectra of vateritic calcium carbonate. *Spectrosc. Lett.* **1995**, *28*, 983–995.
[48] Sauer, G. R.; Zunic, W. B.; Durig, J. R.; Wuthier, R. E. Fourier transform Raman spectroscopy of synthetic and biological calcium phosphates. *Calcif. Tissue Int.* **1994**, *54*, 414–420.
[49] Cuscó, R.; Guitián, F.; de Aza, S.; Artús, L. Differentiation between hydroxyapatite and β-tricalcium phosphate by means of μ-Raman spectroscopy. *J. Eur. Ceram. Soc.* **1998**, *18*, 1301–1305.
[50] de Aza, P. N.; Santos, C.; Pazo, A.; de Aza, S.; Cuscó, R.; Artús, L. Vibrational properties of calcium phosphate compounds. *1. Raman spectrum of β-tricalcium phosphate. Chem. Mater.* **1997**, *9*, 912–915.
[51] Li, J. M.; Jansen, J. A.; Walboomers, X. F.; van den Beucken, J. J. J. P. Mechanical aspects of dental implants and osseointegration: A narrative review. *J. Mech. Behav. Biomed. Mater.* **2020**, *103*, 103574.
[52] Wang, L. N.; Meng, Y. F.; Feng, Y. H. Z.; Wang, H. C.; Mao, L. B.; Yu, S. H.; Wang, Z. L. Amorphous precursor-mediated calcium phosphate coatings with tunable microstructures for customized bone implants. *Adv. Healthcare Mater.* **2022**, *11*, 2201248.